Published in final edited form as:
Adv Mater. 2011 November 2; 23(41): 4793–4797. doi:10.1002/adma.201102948.

Multicore Assemblies Potentiate Magnetic Properties of Biomagnetic Nanoparticles

Tae-Jong Yoon,
Center for Systems Biology, Massachusetts General Hospital, Harvard Medical School, 185 Cambridge St, Boston, MA 02114, USA

Department of Applied Bioscience, CHA University, Seoul 135-081, Republic of Korea

Hakho Lee,
Center for Systems Biology, Massachusetts General Hospital, Harvard Medical School, 185 Cambridge St, Boston, MA 02114, USA

Huilin Shao,
Center for Systems Biology, Massachusetts General Hospital, Harvard Medical School, 185 Cambridge St, Boston, MA 02114, USA

Scott A. Hilderbrand, and
Center for Systems Biology, Massachusetts General Hospital, Harvard Medical School, 185 Cambridge St, Boston, MA 02114, USA

Ralph Weissleder
Center for Systems Biology, Massachusetts General Hospital, Harvard Medical School, 185 Cambridge St, Boston, MA 02114, USA

Department of Systems Biology, Harvard Medical School, 200 Longwood Ave., Alpert 536, Boston, MA 02115, USA

Hakho Lee: hlee@mgh.harvard.edu; Ralph Weissleder: rweissleder@mgh.harvard.edu

Biocompatible magnetic nanoparticles (MNPs) that are both stable and amenable to chemical modification with targeting ligands continue to emerge as important materials in biomedical research.[1–5] MNPs provide an efficient contrast mechanism for biological targets; as most biological samples have intrinsically low magnetic susceptibility, only MNP-labeled objects will respond to external magnetic stimuli. Such properties have led to the widespread use of MNPs, for example, in cell sorting and bioseparation,[6, 7] medical diagnosis,[8–10] imaging,[11–14] and therapeutics.[15, 16]

A key application of MNPs is as "T_2-shortening" agents in nuclear magnetic resonance (NMR). By producing local dipole fields with strong spatial variations, MNPs can accelerate the spin-spin relaxation of adjacent water molecules, resulting in faster decay of the ^{1}H NMR signal.[17, 18] Transverse relaxivity (r_2) is defined to measure the potency of MNPs for such effects. MNPs with higher r_2 values are desirable since they can improve detection sensitivity in magnetic resonance (MR)-based sensing and imaging.[19–22] Although r_2 relaxivities can be enhanced by increasing the size of individual particles,[19] this approach

Correspondence to: Hakho Lee, hlee@mgh.harvard.edu; Ralph Weissleder, rweissleder@mgh.harvard.edu.

Supporting Information
Supporting Information is available from the Wiley Online Library or from the author. Details about the experimental methods are included.

often poses technical difficulties; large, single-core MNPs tend to be polydisperse and can aggregate in suspension. An alternative route is to embed multiple magnetic cores into a larger substrate matrix such as silica or polystyrene. This method is appealing as it provides a facile way to increase the overall magnetic content per particle, while still maintaining high colloidal stability. Thus far, however, most reported particles prepared by this approach have shown suboptimal r_2 potencies, since they often consist of a few, separate magnetic cores embedded in a relatively thick shell.[23–28]

Herein, we report on an optimized design for multicore MNPs, capable of achieving maximal r_2 relaxivities near theoretical limits. These new particles consist of a nanoscale cluster of multiple MNPs encapsulated within a thin silica shell. The construct, named nanomagnetic pomegranate (NMP) due to the morphological similarity to its namesake, has a large magnetic content and produce a strong magnetic field on the particle surface, which together enables it to assume high r_2 relaxivity. Most importantly, theoretical modeling has revealed that NMP is an optimal structure for achieving high r_2; through the control of the shell thickness, the r_2 relaxivity could approach the maximum value for a given material. Furthermore, these NMPs also a) facilitate the incorporation of other functional materials (e.g., fluorochromes), b) protect internal components against degradation (e.g., dissolution of magnetic cores at low pH) and photophysical effects (photobleaching), and c) result in an overall reduced polymer-to-metal ratio. As a specific example in the present study, we synthesized dual-functional NMPs for magnetic resonance (MR) as well as fluorescent sensing and imaging. Clusters of manganese (Mn)-doped ferrite MNPs were synthesized and embedded into a thin silica shell infused with fluorescent molecules. The resultant NMPs exhibited high r_2 relaxivity (695 s^{-1} m_M^{-1} [metal]), close to their theoretical limit (759 s^{-1} m_M^{-1} [metal]), and showed excellent photostability. The prepared NMPs were subsequently applied to an NMR-based detection system to demonstrate their use in identifying soluble biomarkers and mammalian cells in vitro. Dual imaging capacity was also demonstrated using MR and fluorescent imaging in vivo.

We initially synthesized monocrystallline Mn-doped ferrite cores ($MnFe_2O_4$; Mn-MNPs) and enlarged them iteratively through a seed-growth method.[19, 29] Mn-MNP was chosen as the core material for its high magnetization among ferrite crystals.[21] The particles were prepared by thermally decomposing a mixture of $Fe(acac)_3$ and $Mn(acac)_2$ in 1,2-hexadecanediol. The as-synthesized particles were then mixed and reacted with additional precursors to allow for particle growth (see Supporting Information for details). Using this procedure, we obtained highly monodisperse Mn-MNPs (size variations < 5%) up to a diameter of 16 nm (Figure 1a). The prepared Mn-MNPs were subsequently rendered water-soluble by coating their surface with dimercaptosuccinic acid (DMSA) via ligand exchange.

To assemble the magnetic cores prior to silica coating (Scheme 1), the DMSA-coated cores (16 nm Mn-MNPs; Scheme 1 a) were modified further with polyvinylpyrrolidone (PVP, M_w = 55 kDa). PVP-treated Mn-MNPs were then suspended in a mixture of ethanol and acetone (10/1 v/v) to induce particle clustering (Scheme 1 b). Next, tetraethyl orthosilicate (TEOS) was injected to facilitate formation of a silica shell around individual MNP-clusters through the Stöber process.[30] By changing the molar ratio of Mn-MNPs and TEOS (Figure 1b and Figure S1, Supporting Information), the shell thickness could be varied from 9 to 140 nm. To enable optical imaging in deep tissues, we also incorporated near infrared fluorochromes (e.g., VivoTag680; VT680) during shell growth (Scheme 1 c). An additional thin silica-coating was applied to completely shield the dye molecules (Scheme 1 d). NMPs were further treated with 2-[methoxy(polyethyleneoxy)propyl]trimethoxy silane (Si-PEG) to improve their hydrophilicity and with 3-aminopropyltriethyoxysilane (APS) to generate primary amine (NH_2) termination for surface chemical modification.

All core Mn-MNPs remained intact following clustering and silica-coating steps, as confirmed by transmission electron microscopy (TEM; Figure 1b). The average diameter of the MNP clusters was ≈68 nm. The estimated number of Mn-MNP cores per NMP was ≈57, assuming close-stacking of spheres and a packing ratio of ≈0.74. X-ray powder diffraction (XRD) of NMPs revealed the same peaks for inverse spinel structure as observed for untreated Mn-MNPs (Figure 1c), providing further evidence that the size and crystallinity of the core particles is preserved. Note that the broad background at low angles is due to the amorphous nature of the silica shell. Subsequent magnetic measurements showed that all NMPs were superparamagnetic at temperature T = 300 K (Figure 1d and Figure S2, Supporting Information) with similar magnetization (≈100 emu g^{-1} [Fe+Mn]) to the core particles.

NMPs (diameter = 86 nm) showed excellent dispersion in aqueous media without sedimentation. Cytotoxicity assays confirmed the biocompatibility of NMPs, with cell viability remaining at >90% even at the highest metal dose tested (400 μg mL^{-1} [Fe+Mn]; Figure S3, Supporting Information). To attach targeting moieties to the NMP surface, we employed a recently described bioorthogonal conjugation that is based on the Diels–Alder cycloaddition between tetrazine and norbornene (Figure S4, Supporting Information).[31] This strategy provides an efficient method for bioconjugation due to its fast reaction, modular approach, and formation of covalent bonds. Tetrazine was loaded onto NH_2-terminated NMPs through the formation of amide bonds. Targeting molecules (e.g., antibodies) prelabeled with norbornene were then added to tetrazine-active NMPs. On average, ≈100 antibodies could be immobilized onto each NMP in under an hour.

Next, we characterized the r_2 of NMPs and core Mn-MNPs (Figure 2a and Table S1, Supporting Information) at the polarizing magnetic field B = 0.5 T. For Mn-MNPs, we found that the relaxivity increased with the particle radius (a). In contrast, whilst all NMPs maintained higher r_2 values than single-cored particles, they exhibited rather different r_2 behavior. As the particle size increased, r_2 values of NMPs were seen to first plateau and then decrease. These r_2 trends can be explained by the relaxation model based on chemical exchange (see Supporting Information for details).[32] With a sufficiently small particle radius (a < 13 nm for Mn-MNPs), the diffusional motion of water molecules is fast enough to average out the magnetic fields produced by MNPs (motional averaging). The r_2 value in this regime is proportional to the residence time (τ_d), during which water molecules are under the influence of a magnetic particle. With $\tau_d \approx a^2 / D$, where D is the diffusion coefficient, r_2 is thus proportional to a^2, as reflected in the observed r_2 behavior (motional averaging regime in Figure 2a; see Global r_2 model in the Supporting Information). As τ_d increases further with growing particle size, the averaging effect subsides and MNPs approximate that of randomly distributed stationary objects.[33] The corresponding relaxation mechanism, known as static dephasing, not only predicts that r_2 relaxivity is independent of particle size ($r_2 \sim a^0$), but importantly sets the absolute limit on r_2 for a given material (see Global r_2 model). On account of their large size, NMPs with a < 150 nm fall within the limits of the static dephasing regime. The measured r_2 was ≈695 s^{-1} m_M^{-1} [metal], which is approaching the predicted limit of 759 s^{-1} m_M^{-1} [metal] for NMPs. Note that it is practically impossible for single-core MNPs to reach the static dephasing regime. For Mn-MNPs to enter the static dephasing regime, they must have a minimum radius of >13 nm; such MNPs are not only difficult to synthesize but also spontaneously aggregate due to magnetic interactions. As the particle diameter increases beyond the static dephasing regime, the r_2 of NMPs begins to decrease ($r_2 \sim a^{-1}$) as the magnetic field generated by the particles diminishes due to their thick shell (weak magnetic region in Figure 2a).

The superior r_2 relaxivity of NMPs was further verified by a comparative phantom study (Figure 2b; B = 7 T). Among similarly sized, single-core ferrite particles, Mn-doped ferrite

showed the highest contrast, which corroborated its selection as the magnetic core for NMPs. The thin-shelled (9 nm) NMPs significantly outperformed the Mn-MNPs by producing the same level of contrast but with ≈5 times lower metal concentration. Moreover, the NMPs demonstrated effective contrasting even at very low metal concentration (<0.1 p_M). We also noted that the transverse relaxation time (T_2) of NMPs was highly stable during measurements and exhibited zero artifacts (Figure S5, Supporting Information). Magnetic beads, however, despite being embedded within a large number of MNPs, showed a large T_2-drift due to sedimentation. These results will undoubtably have important implications for both single cell tracking and MR imaging of biomarkers.

We next investigated the possible use of NMPs as dual magnetic and fluorescent agents. Most fluorescent dyes lack the photostability to allow for prolonged longitudinal imaging and often suffer from photobleaching. We reasoned that such limitations could be overcome by embedding organic fluorochromes within a silica matrix (Scheme 1 c) and by adding a second protective shell layer (Scheme 1d) to further isolate dyes from the environment. Indeed, when monitored under intense ultraviolet exposure, layer-protected NMPs showed negligible loss in their fluorescence intensity over time (Figure 3a). In contrast, when dye molecules were left exposed on the particle surface, their intensity dropped to 75% of their initial value; free dyes were entirely bleached after 300 min of exposure. It is likely that the superb photostability proffered by NMPs could be particularly beneficial to time-lapse microscopy. Figure 3b compares laser scanning microscopy images of cancer cells (SkBr3) that have been labeled either with NMP-VT680 conjugated to antibodies (against the cancer marker HER2/*neu*) or with free fluorescent antibodies. As shown, while NMP-VT680 were able to maintain constant emission intensity even under continuous exposure to the light source, the signal from free dyes began to fade within 10 min.

To illustrate the utility of NMPs for biomedical sensing, we applied the particles to the detection of small molecules and mammalian cells using a miniaturized NMR system.[34] The avidin–biotin interaction was used as a model system for molecular recognition. Varying amounts of avidin were added to a solution of biotinylated NMPs, which caused aggregation of the NMPs as well as corresponding increases in T_2 relaxation times (Figure 4a). Due to their higher r_2 relaxivity, NMPs produced larger T_2 changes upon aggregation than did the 16 nm Mn-MNPs. Accordingly, the avidin-detection limit for NMPs was ≈1 p_M, significantly lower than that for Mn-MNPs (≈20 p_M). For the cellular assay, cancer cells (SkBr3) were first targeted with HER2-specific NMPs, and detected in a 1 μL NMR sample chamber. NMPs were shown capable of detecting cancer cells at the single-cell level (Figure 4b). We next demonstrated the efficacy of NMPs as dual-modality imaging agents (Figure 4c). Magnetofluorescent NMPs were intravenously injected (10 mg [metal] kg^{-1}) into mice, and the animals were subsequently subject to magnetic resonance imaging (MRI) and fluorescence-mediated tomography (FMT). MR images taken at 24 h post-injection showed significant darkening in organs containing phagocytic cells (e.g., liver, spleen), while corresponding FMT images of the same organs revealed high fluorescent signals. When data were fused in three dimensions, both imaging modalities showed excellent signal congruence. Signal intensities under both MRI and FMT gradually diminished, eventually returning to normal within 3 d. These experiments thus serve not only to verify the beneficial use of NMPs for accurate diagnosis through dual-channel imaging, but also the biocompatibility of NMPs for in vivo applications.

In summary, NMP represents a strategy for preparing highly potent and functional magnetic nanomaterials. There are two major advantages for the NMP construct. First, for a given magnetic material, NMPs are able to achieve maximum r_2 relaxivity. This is made possible by the large number of magnetic cores and by the optimal particle size, which together lead the NMPs to fall within the static dephasing regime. Second, the core/shell approach

employed for NMP synthesis provides a facile method for integrating specific components beneath a protective layer. The silica shell in particular renders the particles highly soluble in aqueous media and simplifies surface conjugation. As a proof-of-concept, we prepared NMPs for dual sensing (MRI and FMT) by incorporating Mn-doped ferrite together with fluorescent dyes. This concept, however, could be readily extended to other MNPs of higher magnetization (e.g., Fe, CoFe), which would further improve the r_2 relaxivity. It is also conceivable that other types of nanoparticles, metallic or semiconducting,[35] could be incorporated along with the MNPs for multimodal imaging and/or therapeutic treatments.

Supplementary Material

Refer to Web version on PubMed Central for supplementary material.

Acknowledgments

T.J.Y. and H.L. contributed equally to this work. The authors thank: C. Ross (MIT) for his generous support in performing magnetic measurements; P. Waterman, J. Donahoe, G. Wojtkiewicz, J. Figueiredo, J. Chen, and M. Nahrendorf for assistance in MRI and FMT; N. Sergeyev for synthesizing CLIO; and Y. Fisher-Jeffes for reviewing the manuscript. This work was supported in part by National Institute of Health Grants R01-EB0044626, R01-EB010011, P50 grant P50CA86355, CCNE contract U54CA151884, and TPEN contract HHSN268201000044C.

References

1. Jun YW, Seo JW, Cheon J. Acc. Chem. Res. 2008; 41:179. [PubMed: 18281944]
2. Kim J, Piao Y, Hyeon T. Chem. Soc. Rev. 2009; 38:372. [PubMed: 19169455]
3. Laurent S, Forge D, Port M, Roch A, Robic C, Vander Elst L, Muller R. Chem. Rev. 2008; 108:2064. [PubMed: 18543879]
4. Frey N, Peng S, Cheng K, Sun S. Chem. Soc. Rev. 2009; 38:2532. [PubMed: 19690734]
5. Cheon J, Lee J. Acc. Chem. Res. 2008; 41:1630. [PubMed: 18698851]
6. Bao J, Chen W, Liu T, Zhu Y, Jin P, Wang L, Liu J, Wei Y, Li Y. ACS Nano. 2007; 1:293. [PubMed: 19206679]
7. Park H, Schadt MJ, Wang L, Lim I, Njoki P, Kim SH, Jang M, Luo J, Zhong C. Langmuir. 2007; 23:9050. [PubMed: 17629315]
8. Gaster R, Hall D, Nielsen C, Osterfeld S, Yu H, Mach K, Wilson R, Murmann B, Liao J, Gambhir S, Wang S. Nat. Med. 2009; 15:1327. [PubMed: 19820717]
9. Lee H, Sun E, Ham D, Weissleder R. Nat. Med. 2008; 14:869. [PubMed: 18607350]
10. Yang J, Gunn J, Dave S, Zhang M, Wang Y, Gao X. Analyst. 2008; 133:154. [PubMed: 18227935]
11. Harisinghani M, Barentsz J, Hahn P, Deserno W, Tabatabaei S, Van De Kaa CH, De La Rosette J, Weissleder R. New Engl. J. Med. 2003; 348:2491. [PubMed: 12815134]
12. Shapiro EM, Skrtic S, Sharer K, Hill JM, Dunbar CE, Koretsky AP. Proc. Natl. Acad. Sci. USA. 2004; 101:10901. [PubMed: 15256592]
13. Rogers WJ, Meyer C, Kramer C. Nat. Clin. Pract. Cardiovasc. Med. 2006; 3:554. [PubMed: 16990841]
14. Thu MS, Najbauer J, Kendall S, Harutyunyan I, Sangalang N, Gutova M, Metz M, Garcia E, Frank R, Kim S, Moats R, Aboody K. PLoS One. 2009; 4:e7218. [PubMed: 19787043]
15. Jain T, Richey J, Strand M, Leslie-Pelecky DL, Flask C, Labhasetwar V. Biomaterials. 2008; 29:4012. [PubMed: 18649936]
16. Mccarthy J, Weissleder R. Adv. Drug Delivery Rev. 2008; 60:1241.
17. Gillis P, Koenig S. Magn. Reson. Med. 1987; 5:323. [PubMed: 2824967]
18. Koenig S, Kellar KE. Magn. Reson. Med. 1995; 34:227. [PubMed: 7476082]
19. Lee H, Yoon T, Figueiredo J, Swirski F, Weissleder R. Proc. Natl. Acad. Sci. USA. 2009; 106:12459. [PubMed: 19620715]
20. Lee H, Yoon T, Weissleder R. Angew. Chem. Int. Ed. 2009; 48:5657.

21. Lee J, Huh Y, Jun YW, Seo JW, Jang J, Song H, Kim S, Cho E, Yoon H, Suh JS, Cheon J. Nat. Med. 2007; 13:95. [PubMed: 17187073]
22. Yoon T, Lee H, Shao H, Weissleder R. Angew. Chem. Int. Ed. 2011; 50:4663.
23. Kim J, Kim H, Lee N, Kim T, Kim H, Yu T, Song I, Moon W, Hyeon T. Angew. Chem. Int. Ed. 2008; 47:8438.
24. Taboada E, Gich M, Roig A. ACS Nano. 2009; 3:3377. [PubMed: 19824669]
25. Taboada E, Solanas R, Rodríguez E, Weissleder R, Roig A. Adv. Funct. Mater. 2009; 19:2319.
26. Yoon T, Yu KN, Kim E, Kim J, Kim B, Yun SH, Sohn B, Cho MH, Lee JK, Park S. Small. 2006; 2:209. [PubMed: 17193022]
27. Yang H, Zhuang Y, Sun Y, Dai A, Shi X, Wu D, Li F, Hu H, Yang S. Biomaterials. 2011; 20:722.
28. Tan H, Xue JM, Shuter B, Li X, Wang J. Adv. Funct. Mater. 2010; 20:722.
29. Sun S, Zeng H, Robinson D, Raoux S, Rice PM, Wang SX, Li G. J. Am. Chem. Soc. 2004; 126:273. [PubMed: 14709092]
30. Stöber W, Fink A, Bohn E. J. Colloid Interface Sci. 1968; 26:62.
31. Devaraj N, Weissleder R, Hilderbrand S. Bioconjugate Chem. 2008; 19:2297.
32. Brooks RA. Magn. Reson. Med. 2002; 47:388. [PubMed: 11810684]
33. Yablonskiy D, Haacke E. Magn. Reson. Med. 1994; 32:749. [PubMed: 7869897]
34. Issadore D, Min C, Liong M, Chung J, Weissleder R, Lee H. Lab Chip. 2011; 11:2282. [PubMed: 21547317]
35. Yi DK, Selvan S, Lee S, Papaefthymiou G, Kundaliya D, Ying J. J. Am. Chem. Soc. 2005; 127:4990. [PubMed: 15810812]

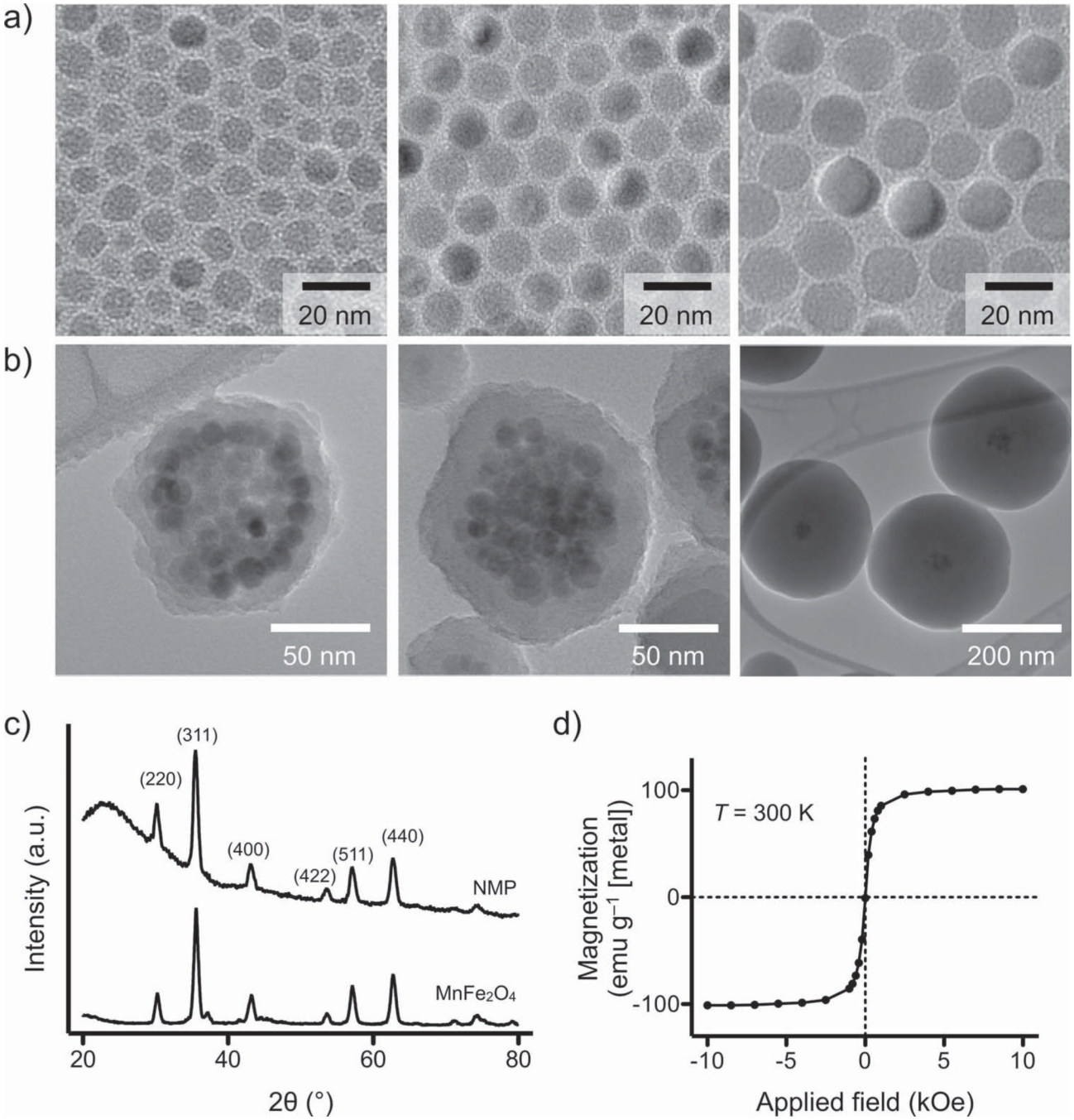

Figure 1.

Synthesis and characterization of NMP. a) Mn-doped ferrite crystals were prepared as core MNPs. These core particles were enlarged up to a diameter of 16 nm through seed-mediated growth. All Mn-MNPs had a narrow size distribution and consisted of a single domain. b) NMPs of different sizes were synthesized by encapsulating a cluster of Mn-MNPs (diameter 16 nm) within a silica shell of varying thickness. The estimated number of core Mn-MNPs per NMP was =57. While keeping the same cluster size, the shell thickness was varied from 9 to 140 nm. c) XRD demonstrated that NMPs exhibited identical peak patterns to their unmodified core Mn-MNPs; this confirmed that the cores are preserved during the silica-coating step. The broad background in NMP signal is due to the amorphous nature of the

silica shell. d) At T = 300 K, NMPs are superparamagnetic and their saturation magnetization (100 emu g^{-1} [metal]) is similar to that of 16 nm Mn-MNPs (101 emu g^{-1} [metal]).

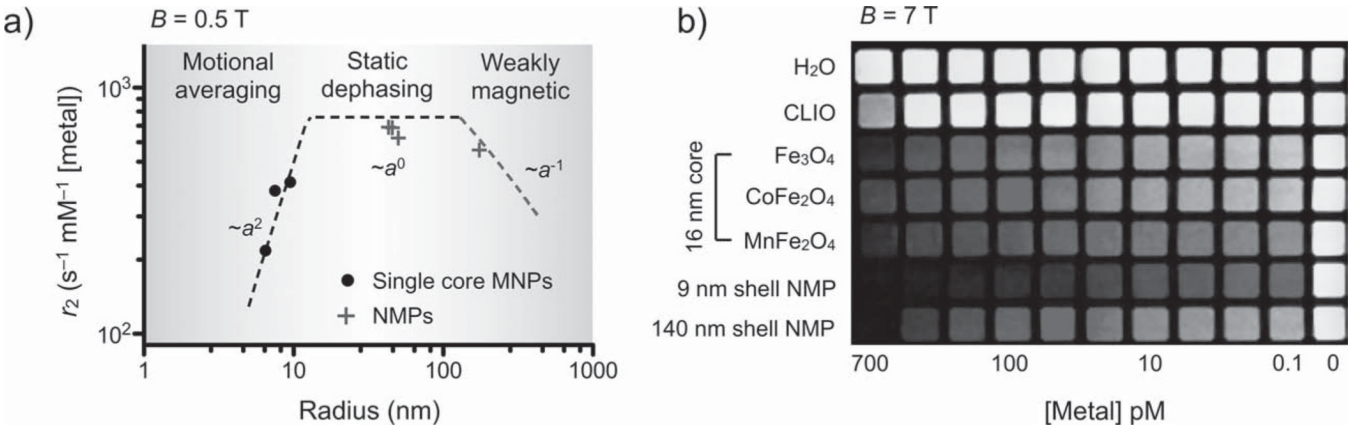

Figure 2.

Characterization of r_2. a) The r_2 values of NMPs and single core Mn-MNPs (at 0.5 T) were compared as a function of particle radius *a*. While the r_2 values of Mn-MNPs increased steeply with increasing particle size ($\sim a^2$), the r_2 values for NMPs initially showed little dependence on particle size ($\sim a^0$) or showed a gradual decrease at larger sizes ($\sim a^{-1}$). Theoretical modeling, based on chemical exchange and static dephasing, was able to accurately describe the observed r_2-behavior (dotted lines). Due to their small particle size, Mn-MNPs fell within the motional averaging regime. Most NMPs were in the static dephasing regime with the exception of thick-shelled NMPs, which fell into the weak-magnetic regime. Importantly, the prepared NMPs showed the highest r_2 value (695 s^{-1} m_M^{-1} [metal]), approaching that of the theoretical limit set by the static dephasing model. b) Phantom images (B = 7.0 T) verified the superiority of NMPs as a MR contrasting agent. Note that the Mn-MNPs (used as the NMP cores) were also superior to similarly sized cobalt ferrite ($CoFe_2O_4$) and ferrite (Fe_3O_4) MNPs, as well as to the conventionally used CLIO (cross-linked iron oxide).

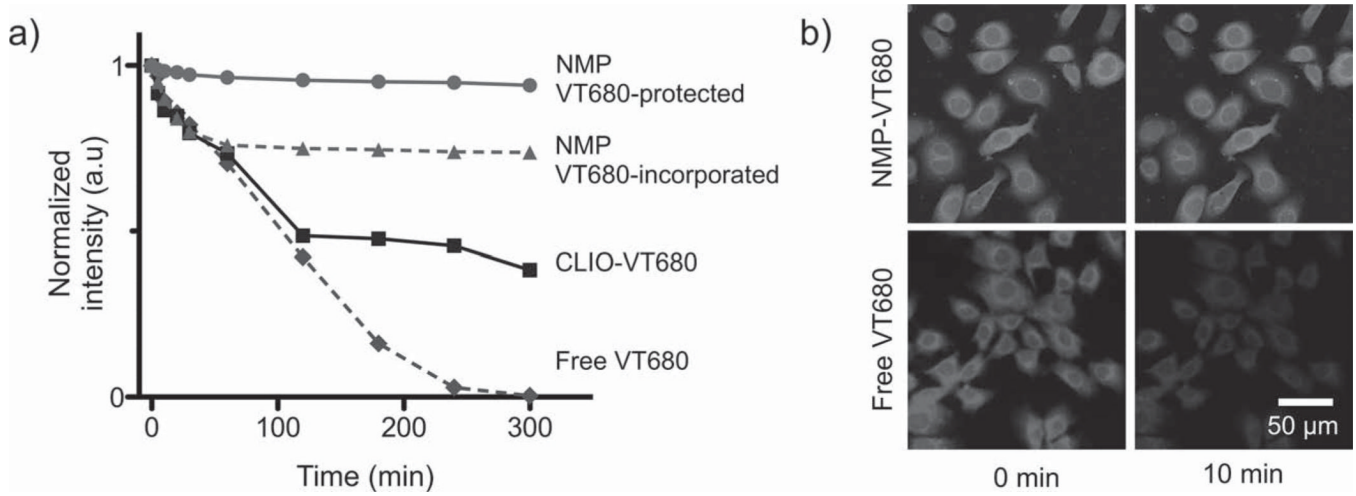

Figure 3.

Optical properties of NMPs. a) Photostability of NMPs and other imaging agents were evaluated by monitoring their fluorescence after continuous exposure to ultraviolet light. Signal loss was found to be inversely proportional to the protection level of the dye molecules against the media. NMP-enclosed dye molecules, which had an extra protective silica shell, showed the best stability and least photobleaching (maintaining >97% of their initial intensity). Particles with dyes exposed were less stable, whereas free dyes showed the fastest decline in signal intensity. b) The superb optical stability offered by the NMPs will likely be of enormous benefit to time-lapse high-resolution microscopy, which requires long exposure of samples to an intense light source. Cells targeted with NMP-VT680, for example, showed little change in signal over 1 h under a laser scanning microscope. For cells labeled with free dyes, however, the fluorescence intensity dropped by > 50% in 10 min.

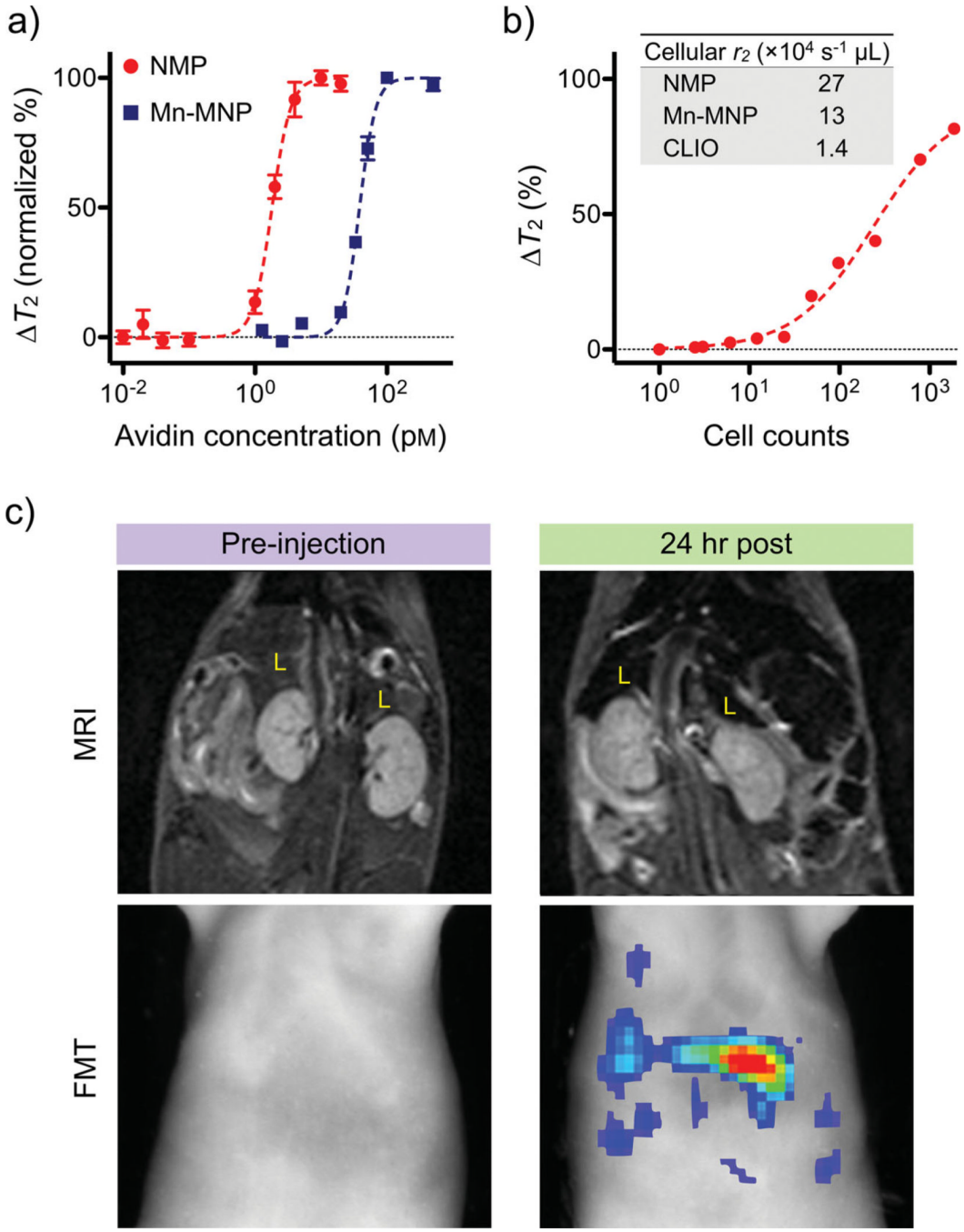

Figure 4.

Biological utility of NMPs. a) Small molecule detection was demonstrated using the avidin–biotin system as a model. Biotinylated NMPs were mixed with varying amounts of avidin, which caused aggregation of NMPs and corresponding changes in T_2 relaxation times. The high r_2 relaxivity of NMPs enabled extremely sensitive detection (≈1 pM of avidin), whereas the detection sensitivity with Mn-MNPs was ≈20-fold lower (20 pM). b) Cancer cells (SkBr3) targeted with HER2/*neu*-specific NMPs could be detected in 1 μL sample volumes, and the detection limit was near single-cell level. The inset table compares the cellular relaxivities of different particle preparations. c) NMPs incorporating near-infrared dyes (NMP-VT680) were used as dual in vivo imaging agents. Mice received intravenous

injections of NMP-VT680 before undergoing both magnetic resonance imaging (MRI) and fluorescent-mediated tomography FMT). Due to large amounts of phagocytic cells, the liver (L) showed decreased signal intensity with MRI, while under FMT, the liver showed high fluorescent signals.

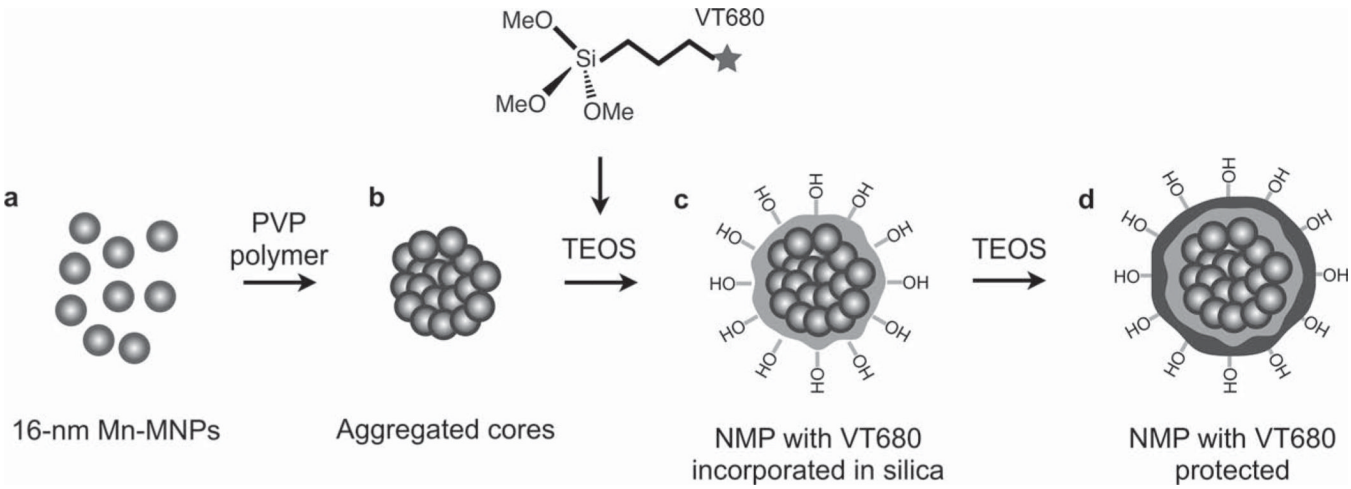

Scheme 1.

Synthesis route of NMP. a) 16 nm Mn-MNPs were coated with DMSA and dispersed in water. b) DMSA-coated Mn-MNPs were then treated with PVP and induced to form a nanoscale cluster. c) The clusters were encapsulated in silica by polymerizing TEOS via the Stöber process. A near infrared dye (VT680) was co-injected at this point to allow incorporation of the dye into the silica shell. d) The Stöber process was repeated to allow another layer of silica to form, protecting the dye from the external environment.